

Wavenumber-Division Multiplexing in Line-of-Sight Holographic MIMO Communications

Luca Sanguinetti, *Senior Member, IEEE*, Antonio Alberto D'Amico, Merouane
Debbah, *Fellow, IEEE*

Abstract

The ultimate performance of any wireless communication system is limited by electromagnetic principles and mechanisms. Motivated by this, we start from the first principles of wave propagation and consider a multiple-input multiple-output (MIMO) representation of a communication system between two spatially-continuous volumes of arbitrary shape and position. This is the concept of holographic MIMO communications. The analysis takes into account the electromagnetic noise field, generated by external sources, and the constraint on the physical radiated power. The electromagnetic MIMO model is particularized for a system with parallel linear sources and receivers in line-of-sight conditions. Inspired by orthogonal-frequency division-multiplexing, we assume that the spatially-continuous transmit currents and received fields are represented using the Fourier basis functions. In doing so, a wavenumber-division multiplexing (WDM) scheme is obtained whose properties are studied with the conventional tools of linear systems theory. Particularly, the interplay among the different system parameters (e.g., transmission range, wavelength, and sizes of source and receiver) in terms of number of communication modes and level of interference is studied. Due to the non-finite support of the electromagnetic channel, we prove that the interference-free condition can only be achieved when the receiver size grows to infinity. The spectral efficiency of WDM is evaluated via the singular-value decomposition architecture with water-filling and compared to that of a simplified architecture, which uses linear processing at the receiver and suboptimal power allocation.

Index Terms

High-frequency communications, wavenumber-domain multiplexing, holographic MIMO communications, electromagnetic channels, free-space line-of-sight propagation, degrees-of-freedom, spectral efficiency.

I. INTRODUCTION

In the quest for ever-increasing data rates, it is natural to continue looking for more bandwidth, which in turn pushes the operation towards higher frequencies than in the past. The current

L. Sanguinetti and A. A. D'Amico are with the Dipartimento di Ingegneria dell'Informazione, University of Pisa, Pisa, Italy.
M. Debbah is with the Mathematical and Algorithmic Sciences Lab, Huawei Technologies Co., Ltd., France.

frontier is in bands up to 86 GHz. However, there is at least 50 GHz of suitable spectrum in the range 90–200 GHz and another 100 GHz in the range 220–320 GHz. These bands are commonly referred to as sub-THz bands and are currently receiving attention for a large variety of emerging applications [1]. As we move up towards high frequencies, the transmission range necessarily shrinks and line-of-sight (LoS) propagation becomes predominant. Classical results in the multiple-input multiple-output (MIMO) literature teach that spatial multiplexing is inevitably compromised in LoS propagation [2]. To understand why this is not the case, recall that such classical results rely on the planar wavefront approximation [3]; that is, the antenna elements experience roughly the same propagation pathloss. This approximation becomes inadequate at high frequencies. Since the wavelength reduces dramatically and the transmission range tends to be short, the wave curvature over the array is no longer negligible and the LoS MIMO channel matrix becomes of high rank [3]–[7]. By properly modeling the wave curvature over the array, one can compute the effective number η of degrees-of-freedom (DoF), which represents the number of independent data streams that can be reliably sent over the channel in the high signal-to-noise regime. For the two parallel line segments illustrated in Fig. 1, if $L_s, L_r \ll d$ we have that (e.g., [8])

$$\eta = \frac{L_s L_r}{\lambda d} \quad (1)$$

which can also be expressed in terms of the solid angles $\Omega_r = L_r/d$ and $\Omega_s = L_s/d$. This result is derived by using the so-called paraxial approximation [8], which follows from elementary diffraction theory.

Motivated by the need of capturing the fundamental properties of wave propagation in wireless communications, we introduce the MIMO representation of a communication system between two *spatially-continuous* volumes of arbitrary shape and position. The model is developed on the basis of prior analyses in electromagnetic theory (e.g., [8]–[11]). Particularly, starting from the Maxwell’s equations describing electromagnetic fields in any known (i.e., deterministic) channel medium, the MIMO model is obtained by representing the spatially-continuous transmit currents and received fields with arbitrary basis sets of functions. This is the concept of *holographic* communications [12]–[14]; that is, the capability to generate any current density distribution (in order to obtain the maximum flexibility in the design of the radiated electromagnetic field) and to weight the impinging electric field according to a desired function. The analysis takes into account the electromagnetic nature of noise fields generated by external sources [10], and

emphasizes the relation between the energy of transmit currents and the physical radiated power. The ultimate performance limit of such MIMO model with spatially-uncorrelated Gaussian noise is known [8]–[10] and can be achieved by using the eigenfunctions of channel operators as basis sets. In analogy to classical analysis of time- and band-limited systems, the optimal eigenfunctions take the form of prolate spheroidal wave functions [15], whose computation and implementation are in general prohibitive [16]. Our contribution here is thus not to look at the fundamental limits, which are known (under the aforementioned conditions), but to provide a unified representation of the electromagnetic wave communication problem, which can be directly used by communication theorists to design and study implementable (from a technological point of view) communication schemes. This is exactly at the basis of the major contribution of this paper, which consists in particularizing the developed model for the LoS system in Fig. 1 and in proposing a novel wavenumber-division multiplexing (WDM) scheme, inspired by orthogonal-frequency division-multiplexing (OFDM). This is achieved by assuming that the spatially-continuous transmit currents and received fields are represented using the Fourier basis functions, which can be efficiently implemented at the electromagnetic level by means of lens antenna arrays or metasurfaces (e.g., [17], [18]). The properties of WDM (in terms of number of communication modes and level of interference) and the functional dependence on the different system parameters (e.g., transmission range, wavelength, and sizes of source and receiver) are studied using the conventional tools of linear systems theory. Unlike OFDM, we show that WDM cannot convert the MIMO channel into a set of parallel and independent sub-channels due to the non-finite support (in spatial domain) of the electromagnetic channel response. The orthogonality among the communication modes is achieved only when the size of the receiver grows infinitely large. The singular-value decomposition (SVD) architecture with water-filling is then used to decompose the channel into non-interfering and independent single-input single-output channels. Comparisons are made with simplified architectures, which use linear processing at the receiver only to mitigate the interference in the wavenumber domain.

A. Paper outline and notation

This paper is organized as follows. Section II revisits the very general system model and capacity achieving scheme of MIMO communications, with particular emphasis on LoS propagations. In Section III, first principles of wave propagation are used to introduce an electromagnetic MIMO representation of the communication problem between two volumes of arbitrary shape and

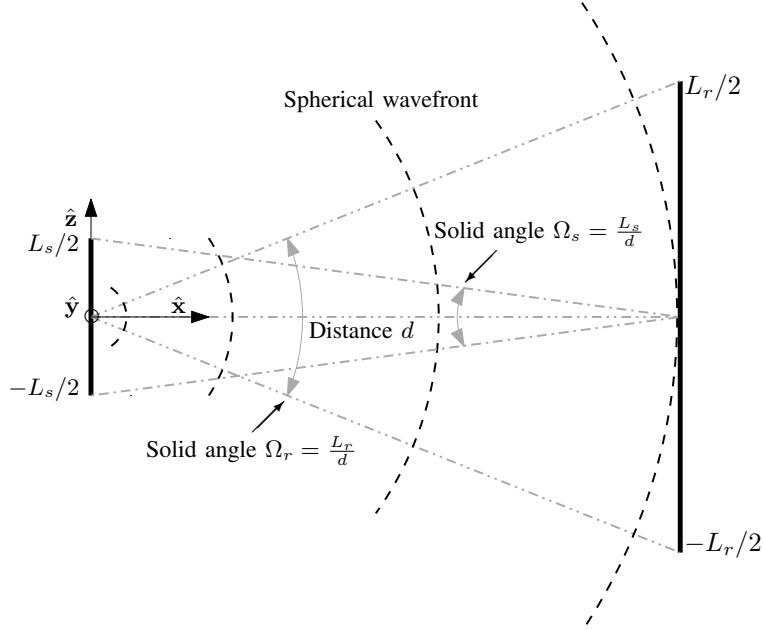


Fig. 1: Illustration of the approach to estimating the number of degrees-of-freedom in the communication between two linear segments of size L_s and L_r , at a distance d . The solid angle Ω_r subtended by the receive line segment of length L_r at a perpendicular distance d is $\Omega_r = L_r/d$. The solid angle Ω_s is similarly given by $\Omega_s = L_s/d$.

position. In Section IV, the developed representation is applied to two parallel one-dimensional electromagnetic apertures and used to propose a WDM scheme, which can be seen as the spatial-counterpart of OFDM. The spectral efficiency of WDM is evaluated in Section V with different transceiver architectures. Some conclusions and future research directions are discussed in Section VI.

We use $\text{rank}(\mathbf{A})$ to denote the rank of matrix \mathbf{A} . For a given vector \mathbf{p} , $\hat{\mathbf{p}}$ is a unit vector along its direction and $\|\mathbf{p}\|$ denotes its magnitude. $\nabla \times$ denotes the curl operation. We denote $\delta(x)$ the Dirac delta function and $\lfloor x \rfloor$ the greatest integer less than or equal to x .

II. MIMO COMMUNICATIONS

A narrowband time-invariant communication system equipped with N_s antennas at the source and N_r antennas at the receiver can be described, at any arbitrary symbol time, by the following discrete-time input-output relation [2]:

$$\mathbf{y} = \mathbf{H}\mathbf{x} + \mathbf{z} \quad (2)$$

where $\mathbf{y} \in \mathbb{C}^{N_r}$ and $\mathbf{x} \in \mathbb{C}^{N_s}$ denote the received and transmitted signal vectors, respectively. The vector \mathbf{x} must satisfy $\mathbb{E}\{\mathbf{x}^H \mathbf{x}\} \leq P$ to constrain the total transmit power. Also, $\mathbf{z} \sim \mathcal{N}_{\mathbb{C}}(\mathbf{0}, \sigma^2 \mathbf{R})$ is the thermal noise and $\mathbf{H} \in \mathbb{C}^{N_r \times N_s}$ is the MIMO channel matrix. Here, the entry H_{nm} represents the gain between the m th source antenna and the n th receive antenna.

A. Capacity and number of degrees-of-freedom

The capacity of the MIMO channel (2) is computed as follows [2]. The received vector \mathbf{y} is premultiplied by \mathbf{L}^{-1} with $\mathbf{R} = \mathbf{L}\mathbf{L}^H$ to obtain $\mathbf{L}^{-1}\mathbf{y}$. Let $\tilde{\mathbf{H}} = \tilde{\mathbf{U}}\tilde{\mathbf{\Lambda}}\tilde{\mathbf{V}}^H$ be the SVD of $\tilde{\mathbf{H}} = \mathbf{L}^{-1}\mathbf{H}$. Hence, $\tilde{\mathbf{y}} = \tilde{\mathbf{U}}^H \mathbf{L}^{-1}\mathbf{y}$ reduces to $\tilde{\mathbf{y}} = \tilde{\mathbf{\Lambda}}\tilde{\mathbf{x}} + \tilde{\mathbf{z}}$ where $\tilde{\mathbf{x}} = \tilde{\mathbf{U}}\mathbf{x}$ and $\tilde{\mathbf{z}} = \tilde{\mathbf{U}}^H \mathbf{L}^{-1}\mathbf{z}$ has independent and identically distributed Gaussian entries, i.e., $\tilde{z}_n \sim \mathcal{N}(0, \sigma^2)$. In scalar form, we have

$$\tilde{y}_n = \tilde{\lambda}_n \tilde{x}_n + \tilde{z}_n, \quad n = 1, \dots, \text{rank}(\tilde{\mathbf{H}}) \quad (3)$$

where $\tilde{\lambda}_n$ are the non-zero singular values. The MIMO channel is decomposed into $\text{rank}(\tilde{\mathbf{H}})$ parallel (non-interfering) and independent single-input single-output channels. The capacity of (3) is thus given by [19]

$$C = \sum_{n=1}^{\text{rank}(\tilde{\mathbf{H}})} \log_2 \left(1 + p_n^* \frac{\tilde{\lambda}_n^2}{\sigma^2} \right) \quad (4)$$

where p_n^* are the waterfilling solutions:

$$p_n^* = \left(\mu - \frac{\sigma^2}{\tilde{\lambda}_n^2} \right)^+ \quad (5)$$

with μ being such that the total transmit power constraint is satisfied, i.e., $\sum_{n=1}^{\text{rank}(\tilde{\mathbf{H}})} p_n^* = P$. Each non-zero $\tilde{\lambda}_n$ corresponds to a *communication mode* of the channel and can potentially be used to transmit a data stream. The number of communication modes determines the channel DoF [2].

B. Line-of-sight channels

The simplest channel model for \mathbf{H} in high-frequency MIMO communications relies on LoS propagation and assume that the source array is located in the *far-field of the receive array*. This condition refers to the propagation range at which the direction of arrival of the signal and the channel gain are approximately the same for all the elements in the array. In this case, \mathbf{H} has

rank one with $\lambda_1 = \sqrt{\beta N_r N_s}$ where β is the propagation path loss. The capacity in bit/s/Hz is thus [2]:

$$C = \log_2 \left(1 + N_r N_s \frac{\beta P}{\sigma^2} \right) \quad (6)$$

which states that, under the far-field LoS assumption, a MIMO system achieves the full array gain $N_r N_s$ but can only transmit a single data stream. This is a direct consequence of the far-field assumption and holds true for any arbitrary array geometry, e.g., linear and planar arrays. When the distance between the transmitter and receiver is of the same order as the size of the arrays, the antenna elements experience large differences in the channel gain due to the varying propagation distances and angles. The far-field assumption breaks down and spherical wave modelling is needed [4]–[7]. In this case, uniform linear arrays can give rise to a channel with N all-equal singular values, provided that $N_r = N_s = N$ and the antenna spacing is $\Delta = \sqrt{\lambda d/N}$ [6]. Similar conditions for a variety of other array geometries can also be found, e.g., [20].

To capture the essence of MIMO communications in different electromagnetic regimes, in the next section we introduce a general MIMO representation of a communication system between two volumes of arbitrary shape and position that is valid for any known channel medium.

III. ELECTROMAGNETIC WAVE COMMUNICATION PROBLEM

Consider two volumes of arbitrary shape and position that communicate through an infinite and homogeneous medium, which is characterized by the scalar frequency- and position-independent permeability $\mu_0 = 4\pi \times 10^{-7}$ [H/m]. An electric current density $\mathbf{j}(\mathbf{s}, t)$ at the source generates an electric field $\mathbf{e}(\mathbf{r}, t)$ in [V/m] at a generic location \mathbf{r} of the receive volume. We consider only monochromatic sources and electric fields of the form

$$\mathbf{j}(\mathbf{s}, t) = \Re\{\mathbf{j}(\mathbf{s})e^{-j\omega t}\} \quad \text{and} \quad \mathbf{e}(\mathbf{r}, t) = \Re\{\mathbf{e}(\mathbf{r})e^{-j\omega t}\}. \quad (7)$$

In this case, Maxwell's equations can be written in terms of the phasor amplitudes $\mathbf{j}(\mathbf{s})$ and $\mathbf{e}(\mathbf{r})$. The sources are assumed to be bounded, so that the current density satisfies

$$\int_{V_s} \|\mathbf{j}(\mathbf{s})\|^2 d\mathbf{s} < \infty \quad (8)$$

which guarantees a bounded radiated power, as shown in Section III-E.

The electric field $\mathbf{y}(\mathbf{r})$ observed inside volume V_r is the sum of the information-carrying electric field $\mathbf{e}(\mathbf{r})$ and a random noise field $\mathbf{n}(\mathbf{r})$, i.e.,

$$\mathbf{y}(\mathbf{r}) = \mathbf{e}(\mathbf{r}) + \mathbf{n}(\mathbf{r}) \quad \mathbf{r} \in V_r \quad (9)$$

where $\mathbf{n}(\mathbf{r})$ is produced by electromagnetic waves that are not generated by the input source. In Cartesian coordinates, $\mathbf{e}(\mathbf{r}) = e_x(\mathbf{r})\hat{\mathbf{x}} + e_y(\mathbf{r})\hat{\mathbf{y}} + e_z(\mathbf{r})\hat{\mathbf{z}}$ and $\mathbf{n}(\mathbf{r}) = n_x(\mathbf{r})\hat{\mathbf{x}} + n_y(\mathbf{r})\hat{\mathbf{y}} + n_z(\mathbf{r})\hat{\mathbf{z}}$ where $\hat{\mathbf{x}}, \hat{\mathbf{y}}$ and $\hat{\mathbf{z}}$ are the unit vectors, independent of position \mathbf{r} .

A. The Green function and signal-carrying electric field

The electric current density $\mathbf{j}(\mathbf{s})$ at any arbitrary source point \mathbf{s} inside volume V_s generates, at any arbitrary point \mathbf{r}' , an electric field $\mathbf{e}(\mathbf{r}')$ that locally obeys the vector wave equation [21, Eq. (1.3.44)]

$$\nabla \times \nabla \times \mathbf{e}(\mathbf{r}') - \kappa^2 \mathbf{e}(\mathbf{r}') = j\omega\mu_0\mathbf{j}(\mathbf{r}') = j\kappa Z_0\mathbf{j}(\mathbf{r}') \quad (10)$$

where $\kappa = \omega/c = 2\pi/\lambda$ is the wavenumber (with c being the speed of light) and $Z_0 = \mu_0 c = 376.73 [\text{Ohm}]$ is the free-space intrinsic impedance. The solution to (10) is given by [21, Eq. (1.3.53)]

$$\mathbf{e}(\mathbf{r}) = j\kappa Z_0 \int_{V_s} \mathbf{g}(\mathbf{r}, \mathbf{s}) \mathbf{j}(\mathbf{s}) d\mathbf{s}, \quad \mathbf{r} \in V_r \quad (11)$$

where [21, Eq. (1.3.51)]

$$\mathbf{g}(\mathbf{r}, \mathbf{s}) = \frac{1}{4\pi} \frac{e^{j\kappa\|\mathbf{r}-\mathbf{s}\|}}{\|\mathbf{r}-\mathbf{s}\|} \left(\mathbf{I} + \frac{\nabla_{\mathbf{r}} \nabla_{\mathbf{r}}^H}{\kappa^2} \right) \quad (12)$$

is the Green's function for the electric field in an unbounded, homogeneous medium. In free-space, under the far-field approximation¹ (i.e. $\|\mathbf{r}-\mathbf{s}\| \gg \lambda$), the Green's function in (12) can be approximated as [22]

$$\mathbf{g}(\mathbf{r}, \mathbf{s}) \approx \frac{1}{4\pi} \frac{e^{j\kappa\|\mathbf{r}-\mathbf{s}\|}}{\|\mathbf{r}-\mathbf{s}\|} (\mathbf{I} - \hat{\mathbf{p}}\hat{\mathbf{p}}^H) \quad (13)$$

where $\hat{\mathbf{p}} = \mathbf{p}/\|\mathbf{p}\|$ and $\mathbf{p} = \mathbf{r} - \mathbf{s}$.

¹The far-field approximation in electromagnetic propagation corresponds to the radiated field that falls off inversely as the distance apart $\|\mathbf{r}-\mathbf{s}\|$. Hence, its power follows the inverse square law.

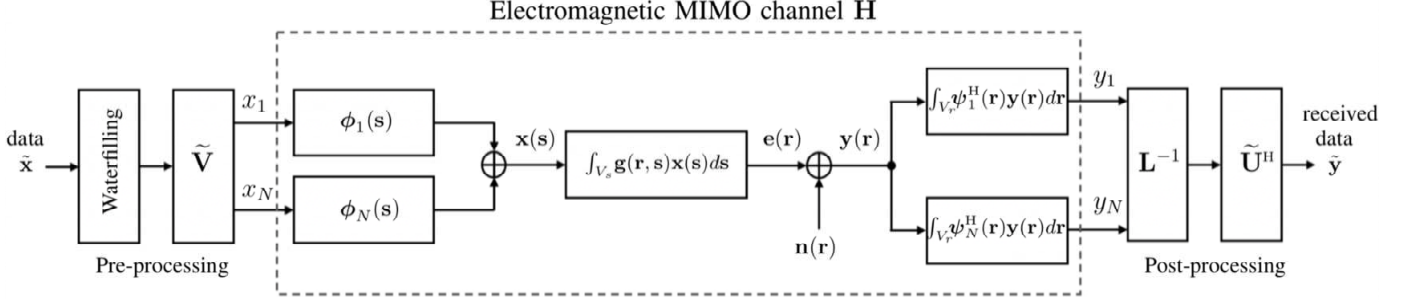


Fig. 2: Optimal transceiver architecture for any choice of vectors $\{\phi_m(\mathbf{s}); m = 1, \dots, N\}$ and $\{\psi_n(\mathbf{r}); n = 1, \dots, N\}$.

B. The noise field

The noise field $\mathbf{n}(\mathbf{r})$ is produced by the incoming electromagnetic waves that are not generated by the source. Suppose that they are generated in the far-field of the receiving volume. Each electromagnetic wave can thus be modelled as a plane wave that reaches the *receiving volume* from an arbitrary elevation angle $\theta_r \in [0, \pi)$ and an arbitrary azimuth angle $\varphi_r \in [-\pi, \pi)$. The noise field $\mathbf{n}(\mathbf{r})$ is thus

$$\mathbf{n}(\mathbf{r}) = \int_{-\pi}^{\pi} \int_0^{\pi} \mathbf{n}(\mathbf{r}, \theta_r, \varphi_r) d\theta_r d\varphi_r \quad (14)$$

where $\mathbf{n}(\mathbf{r}, \theta_r, \varphi_r)$ is defined as

$$\mathbf{n}(\mathbf{r}, \theta_r, \varphi_r) = \mathbf{a}(\theta_r, \varphi_r) e^{j\boldsymbol{\kappa}^T(\theta_r, \varphi_r)\mathbf{r}}. \quad (15)$$

Here,

$$\boldsymbol{\kappa}(\theta_r, \varphi_r) = \frac{2\pi}{\lambda} [\cos \varphi_r \sin \theta_r, \sin \varphi_r \sin \theta_r, \cos \theta_r]^T \quad (16)$$

is the wave vector that describes the phase variation of the plane wave with respect to the three Cartesian coordinates at the receiving volume, $\mathbf{a}(\theta_r, \varphi_r)$ is a zero-mean, complex-Gaussian random process with

$$\mathbb{E}\{\mathbf{a}(\theta_r, \varphi_r) \mathbf{a}^H(\theta'_r, \varphi'_r)\} = \sigma^2 f(\theta_r, \varphi_r) \mathbf{I}_3 \delta(\varphi_r - \varphi'_r) \delta(\theta_r - \theta'_r) \quad (17)$$

and $\sigma^2 f(\theta_r, \varphi_r)$ denotes the noise power angular density with σ^2 being measured in V^2/m^2 . From (14), using (15) and (17) yields

$$\mathbb{E}\{\mathbf{n}(\mathbf{r}') \mathbf{n}^H(\mathbf{r} + \mathbf{r}')\} = \sigma^2 \rho(\mathbf{r}) \mathbf{I}_3 \quad (18)$$

with

$$\rho(\mathbf{r}) = \int_{-\pi}^{\pi} \int_0^{\pi} f(\theta_r, \varphi_r) e^{-j\boldsymbol{\kappa}^T(\theta_r, \varphi_r)\mathbf{r}} d\theta_r d\varphi_r. \quad (19)$$

The above model is valid for any $f(\theta_r, \varphi_r)$. In the case of electromagnetic waves not generated by the source, we can reasonably assume that they are uniformly distributed in the angular domain. This corresponds to an isotropic propagation condition, characterized by

$$f(\theta_r, \varphi_r) = \frac{\sin \theta_r}{4\pi} \quad \theta_r \in [0, \pi), \varphi_r \in [-\pi, \pi). \quad (20)$$

Plugging (20) into (19) yields

$$\rho(\mathbf{r}) = \int_{-\pi}^{\pi} \int_0^{\pi} \frac{\sin \theta_r}{4\pi} e^{-j\boldsymbol{\kappa}^T(\theta_r, \varphi_r)\mathbf{r}} d\theta_r d\varphi_r = \text{sinc}\left(\frac{2\|\mathbf{r}\|}{\lambda}\right). \quad (21)$$

Remark 1. In MIMO communications, the noise samples in (2), taken at arbitrary points \mathbf{r}' and $\mathbf{r} + \mathbf{r}'$, are typically modelled as independent zero-mean and circularly-symmetric Gaussian random variables, i.e., $\rho(\mathbf{r}) = \sigma^2 \delta(\mathbf{r})$. This is not generally the case for noise samples of electromagnetic nature as it follows from (21). It happens only when $\|\mathbf{r}\| = i\lambda/2$, with $i \in \mathbb{Z}$, i.e., all samples of $\mathbf{n}(\mathbf{r})$ must be taken along a straight line at a spacing of an integer multiple of $\lambda/2$.

C. The electromagnetic MIMO channel

Assume that the current density $\mathbf{j}(\mathbf{s})$ is expanded using a set of orthonormal vectors $\{\boldsymbol{\phi}_m(\mathbf{s}); m = 1, \dots, N\}$ with N being the dimension of the input signal space. Without loss of generality, we assume that N is an odd number. Accordingly, we can write

$$\mathbf{j}(\mathbf{s}) = \sum_{m=1}^N \xi_m \boldsymbol{\phi}_m(\mathbf{s}) \quad (22)$$

where the coefficient ξ_m satisfies

$$\xi_m = \int_{V_s} \boldsymbol{\phi}_m^H(\mathbf{s}) \mathbf{j}(\mathbf{s}) d\mathbf{s}. \quad (23)$$

The received field $\mathbf{y}(\mathbf{r})$ in (9) is projected onto an output space of dimension N , spanned by a set of receive orthogonal basis functions $\{\boldsymbol{\psi}_n(\mathbf{r}); n = 1, \dots, N\}$. We can thus represent the projected $\mathbf{y}(\mathbf{r})$ by the coefficients

$$y_n = \int_{V_r} \boldsymbol{\psi}_n^H(\mathbf{r}) \mathbf{y}(\mathbf{r}) d\mathbf{r}. \quad (24)$$

Using (22) – (24), the input-output relationship takes the form

$$y_n = \sum_{m=1}^N H_{nm} x_m + z_n \quad n = 1, \dots, N \quad (25)$$

where

$$x_m = j\kappa Z_0 \xi_m \quad (26)$$

are the effective input samples while

$$z_n = \int_{V_r} \psi_n^H(\mathbf{r}) \mathbf{n}(\mathbf{r}) d\mathbf{r} \quad (27)$$

and

$$H_{nm} = \int_{V_r} \int_{V_s} \psi_n^H(\mathbf{r}) \mathbf{g}(\mathbf{r}, \mathbf{s}) \phi_m(\mathbf{s}) d\mathbf{r} d\mathbf{s}. \quad (28)$$

Letting $\mathbf{y} = [y_1, \dots, y_N]^T$ and $\mathbf{x} = [x_1, \dots, x_N]^T$, we may rewrite (25) in the same matrix form of (2) where $\mathbf{H} \in \mathbb{C}^{N \times N}$ is the channel matrix and $\mathbf{z} = [z_1, \dots, z_N]^T \sim \mathcal{N}_{\mathbb{C}}(\mathbf{0}_N, \sigma^2 \mathbf{R})$ with

$$[\mathbf{R}]_{nm} = \iint_{V_r} \rho(\mathbf{r} - \mathbf{r}') \psi_n^H(\mathbf{r}) \psi_m(\mathbf{r}') d\mathbf{r} d\mathbf{r}' \quad (29)$$

as it follows from (27), by using (18) and (21). Unlike (2), where the entries of \mathbf{H} represent the channel gains from transmit to receive antennas, here they represent the *coupling coefficients* between the source mode m and the reception mode n [8]. The capacity of the described electromagnetic MIMO system is thus given by (4) where the communication modes are obtained by computing the singular value decomposition of $\tilde{\mathbf{H}} = \mathbf{L}^{-1} \mathbf{H}$ with the entries of \mathbf{H} and \mathbf{R} given by (28) and (29), respectively. The capacity achieving transceiver architecture for any choice of vector basis functions $\{\phi_m(\mathbf{s}); m = 1, \dots, N\}$ and $\{\psi_n(\mathbf{r}); n = 1, \dots, N\}$ is reported in Fig. 2, where we have called $\mathbf{x}(\mathbf{s}) = j\kappa Z_0 \mathbf{j}(\mathbf{s})$. Notice that the transceiver operates in two stages. Particularly, the inner stage operates directly at the electromagnetic level since it is responsible for generating at the source the current density distribution $\mathbf{j}(\mathbf{s})$ through the use of functions $\{\phi_m(\mathbf{s}); m = 1, \dots, N\}$ and for weighting at the receiver the electric field $\mathbf{y}(\mathbf{r})$ according to the functions $\{\psi_n(\mathbf{r}); n = 1, \dots, N\}$.

D. The electromagnetic radiated power

In signal processing, the quantity on the left-hand-side of (8) represents the *energy* of the continuous-space signal $\mathbf{j}(\mathbf{s})$. Notice that this is different from the electromagnetic radiated power P_{rad} , which can be computed using the Poynting theorem and integrating the radial component

of the Poynting vector over a sphere of radius $r \rightarrow \infty$ [23, Ch. 14]. In Appendix A, it is shown that P_{rad} can be upper-bounded as follows

$$P_{\text{rad}} \leq Q\mathcal{E}_s \quad (30)$$

where $\mathcal{E}_s = \int_{V_s} \|\mathbf{j}(\mathbf{s})\|^2 d\mathbf{s}$ and

$$Q = \frac{\kappa Z_0}{4\lambda} \sqrt{\iint_{V_s} |\rho(\mathbf{s}_1 - \mathbf{s}_2)|^2 d\mathbf{s}_1 d\mathbf{s}_2} \quad (31)$$

with $\rho(\cdot)$ being defined in (21). The upper-bound in (30) shows that imposing the constraint (8) on the L^2 norm of the source $\mathbf{j}(\mathbf{s})$ amounts to limit the radiated power. On the contrary, bounding P_{rad} does not necessarily lead to a bounded source L^2 norm in (8); e.g., [9].

IV. WAVENUMBER-DIVISION MULTIPLEXING

The optimal approach for the design of the communication system depicted in Fig. 2 consists in selecting the elements of the input basis $\{\phi_n(\mathbf{s}); n = 1, \dots, N\}$ as the eigenfunctions of the channel operator (e.g., [8]–[10])

$$\mathbf{K}_s(\mathbf{s}, \mathbf{s}') = \int_{V_r} \mathbf{g}^H(\mathbf{r}, \mathbf{s}) \mathbf{g}(\mathbf{r}, \mathbf{s}') d\mathbf{r}. \quad (32)$$

This means that

$$\gamma_n \phi_n(\mathbf{s}) = \int_{V_s} \mathbf{K}_s(\mathbf{s}, \mathbf{s}') \phi_n(\mathbf{s}') d\mathbf{s}' \quad (33)$$

where γ_n is the eigenvalue associated to the eigenfunction $\phi_n(\mathbf{s})$. The elements of the output basis $\{\psi_n(\mathbf{r}); n = 1, \dots, N\}$ are simply the channel responses to the functions of the input basis, i.e.,

$$\psi_n(\mathbf{r}) = \int_{V_s} \mathbf{g}(\mathbf{r}, \mathbf{s}) \phi_n(\mathbf{s}) d\mathbf{s}. \quad (34)$$

The above approach is optimal under the assumption that the electromagnetic noise can be modelled as a spatially-uncorrelated Gaussian random field. This may not be the case as it follows from the model described in Section III-B. In addition, we stress that the numerical solution of the eigenfunction problem (33) is in general computationally demanding. Moreover, its implementation is prohibitive not only at the electromagnetic (i.e., analog) level but also in the digital domain. We can reasonably ask ourselves whether there is a pair of basis for which the communication system becomes simple to implement and with a clear physical interpretation. To answer this question, we consider the LoS scenario in Fig. 1 and take inspiration from

a communication system operating over a time-domain dispersive (i.e., frequency selective) channel. The communication over this channel is mathematically equivalent to a time-domain MIMO system. By using the OFDM technology, it can be converted into a frequency-domain communication system that transmits over multiple non-interfering frequency-flat channels. This is simply achieved by using Fourier transform operations and a cyclic prefix technique. The objective of this section is to show that a communication scheme sharing these advantages can be obtained from the electromagnetic MIMO channel in the wavenumber domain. We refer to it as *WDM (wavenumber-division multiplexing)*

A. Review of orthogonal-frequency-division multiplexing

Consider a system that employs N subcarriers with frequency spacing $1/T$ and indices in the set $\{-(N-1)/2, \dots, (N-1)/2\}$ with N being an odd integer. The base-band equivalent time-domain signal transmitted over the interval $0 \leq t \leq T_s$ with $T_s \geq T$ is

$$x(t) = \begin{cases} \frac{1}{\sqrt{T_s}} \sum_{m=1}^N x_m e^{j\frac{2\pi}{T}(m-1-\frac{N-1}{2})t}, & 0 \leq t \leq T_s \\ 0, & \text{elsewhere} \end{cases} \quad (35)$$

where x_m is the data associated to the frequency $f_m = \frac{m-1-(N-1)/2}{T}$. The signal $x(t)$ is sent over a wireless channel with impulse response $g(t)$. Wireless channel responses are causal and incur a finite maximum delay. We thus assume that the support of $g(t)$ is the time interval $0 \leq t \leq T_g$. The received signal $y(t)$, given by

$$y(t) = g(t) \otimes x(t) + z(t) \quad (36)$$

where $z(t)$ is the thermal noise, is observed in $T_g \leq t \leq T_g + T_r$. Accordingly, its Fourier transform, evaluated at f_n , is written as:

$$y_n = \int_{T_g}^{T_g+T_r} y(t) e^{-j\frac{2\pi}{T}(n-1-\frac{N-1}{2})t} dt. \quad (37)$$

If

$$T_s \geq T + T_g \quad \text{and} \quad T_r = T \quad (38)$$

then (37) takes the form [2]:

$$y_n = H_n x_n + z_n \quad (39)$$

where $H_n = G_n T_r / \sqrt{T_s}$, with G_n being the channel response at frequency f_n , and z_n the corresponding noise. The expression in (39) describes a set of N non-interfering (orthogonal) parallel transmissions with different complex-valued attenuation factors. Orthogonality is achieved by setting $T_s \geq T + T_g$ in (38), which amounts to append the so-called cyclic prefix to the transmitted signal so that at the receiver (36) can be viewed as a cyclic convolution in the interval $[T_g, T_g + T_r)$. In the frequency-domain, the cyclic convolution becomes the product of the corresponding Fourier transforms and (39) follows easily. It is worth noticing that the same result is achieved if² the received signal is observed in the interval $[0, T_r)$, and we set

$$T_s = T \quad \text{and} \quad T_r \geq T + T_g. \quad (40)$$

In this case, no cyclic prefix is appended at the transmitter but the received signal is observed over an extended time interval including the support of the channel response. The input-output relationship is analogous to (39) but with

$$H_n = \sqrt{T_s} G_n. \quad (41)$$

Although this is not the way OFDM operates, the implication of the conditions (40) are instrumental for the design and understanding of the WDM communication scheme described below.

B. System and signal model

To simplify the analysis and better highlight the similarities with time-domain communication systems and, in particular, with OFDM, we consider the one-dimensional setup illustrated in Fig. 1, which relies on the following assumption.

Assumption 1. *The source is a segment with the following coordinates:*

$$\{(s_x, s_y, s_z) : s_x = 0, s_y = 0, |s_z| \leq L_s/2\}. \quad (42)$$

The receiver is a segment occupying the following region:

$$\{(r_x, r_y, r_z) : r_x = d, r_y = 0, |r_z| \leq L_r/2, \}. \quad (43)$$

Also, $L_r = \ell L_s$ with $\ell \geq 1$ being an integer.³

²This result will be proved in Appendix C for the proposed scheme.

³Notice that this assumption is needed for the output basis functions to be orthogonal, but it is not strictly necessary.

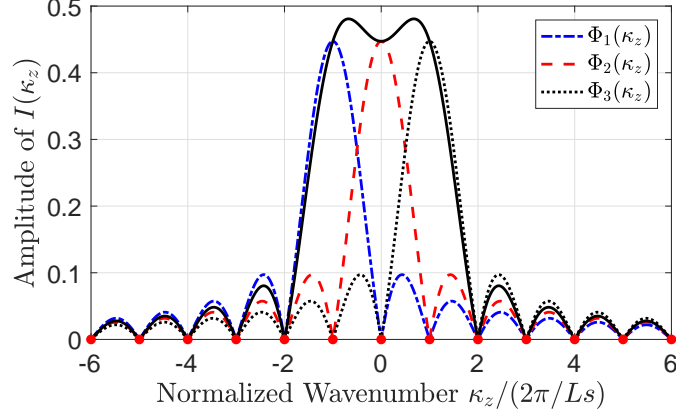


Fig. 3: Amplitude of $I(\kappa_z)$ for $L_s = 0.2$ m and $\lambda = 0.01$ m when $N = 3$ and $\xi_m = 1$ for $m = 1, 2, 3$.

Under Assumption 1, the electric current density is

$$\mathbf{j}(\mathbf{s}) = i(s_z)\delta(s_x)\delta(s_y)\hat{\mathbf{z}} \quad (44)$$

where

$$i(s_z) = \sum_{m=1}^N \xi_m \phi_m(s_z) \quad (45)$$

is a current (measured in amperes). In analogy with an OFDM system, we assume that the basis functions $\{\phi_m(s_z); m = 1, \dots, N\}$ take the form

$$\phi_m(s_z) = \begin{cases} \frac{1}{\sqrt{L_s}} e^{j\frac{2\pi}{L_s} \left(m-1-\frac{N-1}{2}\right) s_z}, & |s_z| \leq \frac{L_s}{2} \\ 0, & \text{elsewhere} \end{cases} \quad (46)$$

such that

$$\xi_m = \int_{-\frac{L_s}{2}}^{\frac{L_s}{2}} i(s_z) \phi_m^*(s_z) ds_z. \quad (47)$$

The wavenumber Fourier transform of $i(s_z)$ is

$$I(\kappa_z) = \int_{-\frac{L_s}{2}}^{\frac{L_s}{2}} i(s_z) e^{-jk_z s_z} ds_z = \sum_{m=1}^N \xi_m \Phi_m(\kappa_z) \quad (48)$$

where

$$\Phi_m(\kappa_z) = \int_{-\frac{L_s}{2}}^{\frac{L_s}{2}} \phi_m(s_z) e^{-jk_z s_z} ds_z = \sqrt{L_s} \text{sinc} \left[\left(\frac{\kappa_z}{2\pi} - \frac{m-1-(N-1)/2}{L_s} \right) L_s \right]. \quad (49)$$

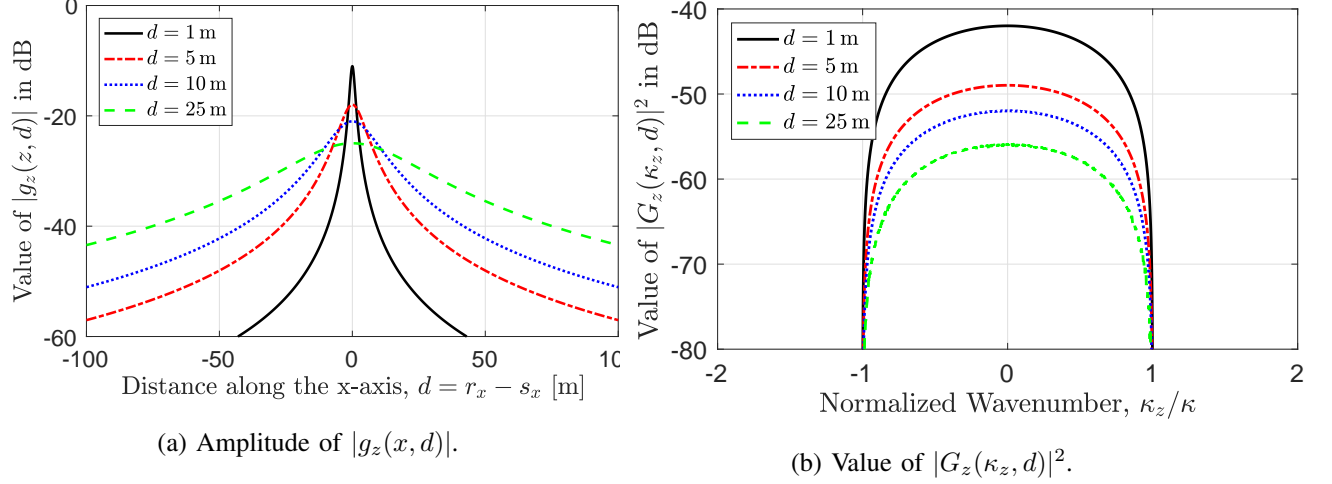


Fig. 4: Behaviour of $|g_z(z, d)|$ and $|G_z(\kappa_z, d)|^2$ for $d = 5, 10$ and 25 m when $\lambda = 0.01$ m (i.e., carrier frequency of 30 GHz).

Fig. 3 plots the amplitude of $I(\kappa_z)$ in (48) for $L_s = 0.2$ m, $\lambda = 0.01$ m and $N = 3$. The distance between the first two nulls of each sinc function is $4\pi/L_s$. Fig. 3 shows that $\Phi_m(\kappa_z)$ has most of its energy in the vicinity of $\frac{2\pi}{L_s}(m - 1 - (N - 1)/2)$. Hence, $I(\kappa_z)$ is practically limited to

$$\left[-\frac{N-1}{2} \frac{2\pi}{L_s}, \frac{N-1}{2} \frac{2\pi}{L_s} \right] \quad (50)$$

and thus has an approximate bandwidth of $\Omega = \frac{\pi N}{L_s}$.

At the receiver, the electric field $\mathbf{y}(\mathbf{r})$ is projected onto the space spanned by the vectors $\boldsymbol{\psi}_n(\mathbf{r})$ given by

$$\boldsymbol{\psi}_n(\mathbf{r}) = \psi_n(r_z) \delta(r_x - d) \delta(r_y) \hat{\mathbf{z}} \quad (51)$$

where, in analogy with OFDM,

$$\psi_n(r_z) = \begin{cases} e^{j \frac{2\pi}{L_s} (n-1 - \frac{N-1}{2}) r_z}, & |r_z| \leq L_r/2 \\ 0, & \text{elsewhere.} \end{cases} \quad (52)$$

The output samples y_n in (24) are expressed in volts. In the wavenumber domain, we have

$$\Psi_n(\kappa_z) = L_r \text{sinc} \left[\left(\frac{\kappa_z}{2\pi} - \frac{n-1 - (N-1)/2}{L_s} \right) L_r \right] \quad (53)$$

where the distance between the first two nulls is now $4\pi/L_r$ and thus inversely proportional to L_r , rather than L_s . From (24), by using (52) we obtain

$$y_n = \int_{-\frac{L_r}{2}}^{\frac{L_r}{2}} \psi_n^*(r_z) y(d, 0, r_z) dr_z = \int_{-\frac{L_r}{2}}^{\frac{L_r}{2}} y(d, 0, r_z) e^{-j \frac{2\pi}{L_s} (n-1 - \frac{N-1}{2}) r_z} dr_z \quad (54)$$

which is simply the n th coefficient of the wavenumber Fourier series expansion of $y(d, 0, r_z)$ taken at $1/L_s$. Clearly, the projection of $\mathbf{y}(\mathbf{r})$ onto the space spanned by (52) allows to only capture the electric field along the z -axis. Notice that (52) are exponential functions whose fundamental spatial frequency is $1/L_s$.

C. The coupling coefficients

Under the system model above, in free-space propagation (28) reduces to

$$H_{nm} = \int_{-\frac{L_r}{2}}^{\frac{L_r}{2}} \int_{-\frac{L_s}{2}}^{\frac{L_s}{2}} g_z(r_z - s_z, d) \psi_n^*(r_z) \phi_m(s_z) ds_z dr_z \quad (55)$$

where $g_z(z, d)$ denotes the $(3, 3)$ th element of $\mathbf{g}(\mathbf{r}, \mathbf{s})$ evaluated at $r_x = d$ and $s_x = s_y = r_y = 0$. From (13), we obtain

$$g_z(z, d) = \frac{d^2}{4\pi} \frac{e^{j\kappa\sqrt{z^2+d^2}}}{(z^2 + d^2)^{3/2}}. \quad (56)$$

In Appendix B, the double integral (55) is rewritten as a single integral to facilitate its evaluation. We call

$$G_z(\kappa_z, d) = \int_{-\infty}^{\infty} g_z(z, d) e^{-j\kappa_z z} dz \quad (57)$$

the Fourier transform in the wavenumber-domain of $g_z(z, d)$, and hence we can write

$$g_z(z, d) = \frac{1}{2\pi} \int_{-\infty}^{\infty} G_z(\kappa_z, d) e^{j\kappa_z z} d\kappa_z. \quad (58)$$

The behaviour of $|g_z(z, d)|$ and $|G_z(\kappa_z, d)|^2$ in dB is illustrated in Fig. 4 for $d = 1, 5, 10$ and 25 m. Unlike time-domain channels, $g_z(z, d)$ is not causal and has an unbounded support. Notice also that $G_z(\kappa_z, d)$ is band-limited in the interval $|\kappa_z| \leq \kappa = 2\pi/\lambda$. The lower the wavelength λ , the larger the spatial-frequency bandwidth. We notice that, for the investigated scenarios, the 3-dB bandwidth of $G_z(\kappa_z, d)$ is approximately $\alpha\kappa$ with $\alpha = 0.6075$.

To quantify the impact of the propagation channel, we reformulate (55) as follows

$$H_{nm} = \int_{-\frac{L_r}{2}}^{\frac{L_r}{2}} \psi_n^*(r_z) \theta_m(r_z) dr_z \quad (59)$$

with

$$\theta_m(r_z) = \int_{-\frac{L_s}{2}}^{\frac{L_s}{2}} g_z(r_z - s_z, d) \phi_m(s_z) ds_z \quad (60)$$

being the m th element of the basis spanning the electric field at the receiver, i.e.,

$$e(d, 0, r_z) = \sum_{m=1}^N x_m \theta_m(r_z). \quad (61)$$

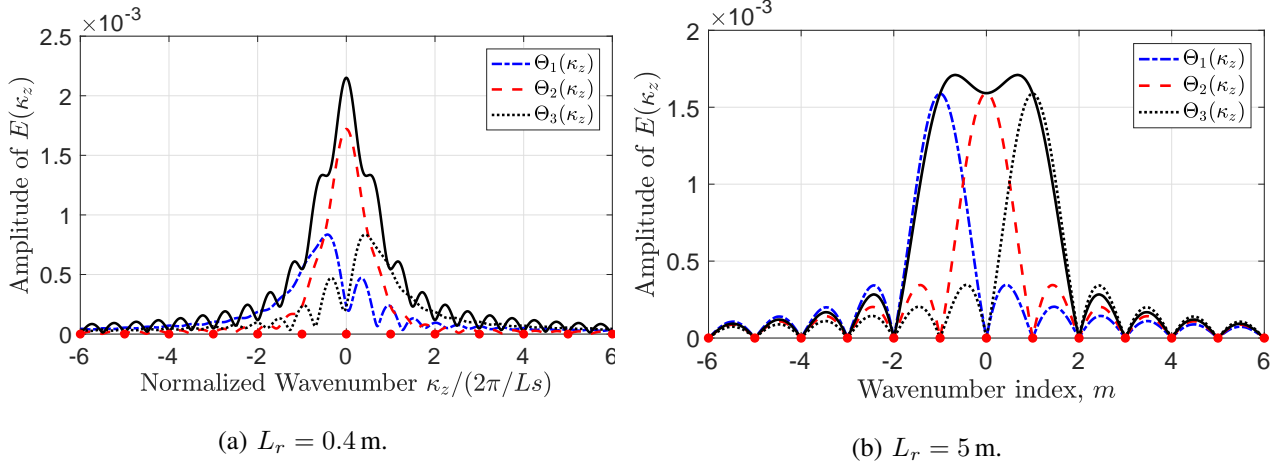


Fig. 5: Amplitude of $E(\kappa_z)$ and $\Theta_m(\kappa_z)$ for $m = 1, 2, 3$ in the same setup of Fig. 3 when $d = 5$ m and $L_r = 0.4$ and 5 m.

We call $E(\kappa_z)$ and $\Theta_m(\kappa_z)$ the Fourier transforms in the wavenumber domain of $e(d, 0, r_z)$ and $\theta_m(r_z)$, respectively. Fig. 5 plots their behaviors in the same setup of Fig. 3 when $d = 5$ m and $L_r = 0.4$ and 5 m. From Fig. 5a, we see that when $L_r = 0.4$ the spectrum of the electric field is highly distorted compared to that in Fig. 3. Moreover, the orthogonality condition among the three communication modes is destroyed. The situation is much different when $L_r = 5$ m. In this case, the electric field is received undistorted over the considered wavenumber interval and the three communication modes are not affected by interference.

By using (58), we may rewrite (55) as

$$H_{nm} = \frac{1}{2\pi} \int G_z(\kappa_z, d) \Psi_n^*(\kappa_z) \Phi_m(\kappa_z) d\kappa_z \quad (62)$$

where $\Phi_m(\kappa_z)$ and $\Psi_n^*(\kappa_z)$ are given by (49) and (53), respectively. Hence, we obtain

$$H_{nm} = \frac{\sqrt{L_s} L_r}{2\pi} \int_{-\infty}^{\infty} G_z(\kappa_z, d) \text{sinc} \left[\left(\frac{\kappa_z}{2\pi} - \frac{n-1-(N-1)/2}{L_s} \right) L_r \right] \times \text{sinc} \left[\left(\frac{\kappa_z}{2\pi} - \frac{m-1-(N-1)/2}{L_s} \right) L_s \right] d\kappa_z \quad (63)$$

In Fig. 6, we illustrate $|H_{nn}/\sqrt{L_s}|^2$ for the same setup of Fig. 4, when $L_r = 1$ and 10 m. As seen, the behaviour of $|H_{nn}/\sqrt{L_s}|^2$ is much different from that of $|G_z(\kappa_z, d)|^2$ in Fig. 4. The number of significant coefficients reduces as d increases. This is exemplified in Fig. 7 where we plot the number \bar{N} of coupling coefficients H_{nn} that resides in the 3-dB bandwidth of $G_z(\kappa_z, d)$ for $L_r = 1$ and 5 m. We see that if $d = 5$ m then $\bar{N} = 3$ and 17 for $L_r = 1$ m and 5 m, respectively.

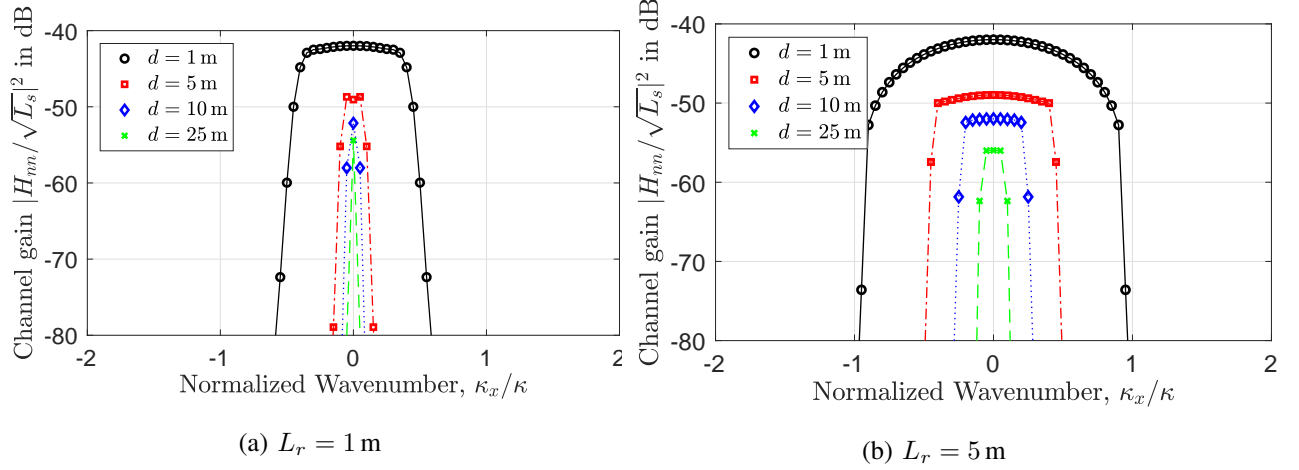


Fig. 6: Behaviour of $|H_{nn}/\sqrt{L_s}|^2$ in (63) in dB in the same setup of Fig. 4 when $L_r = 1$ and 5 m.

These numbers reduce to $\bar{N} = 1$ and 9 when $d = 10$ m. The solid curves are obtained from (1) as (in order to have an odd number of communication modes)

$$2 \left\lfloor \frac{1}{2} \frac{L_s L_r}{\lambda d} \right\rfloor + 1 \quad (64)$$

and represent a good approximation of \bar{N} only when L_r is of the same order of d . This is in agreement with the fact that (1) is valid only in that regime (e.g., [8]). A comparison between Fig. 6a and Fig. 6b shows that, for a given distance d , the coupling coefficient $|H_{nn}/\sqrt{L_s}|^2$ tends to the sampled version of $|G_z(\kappa_z, d)|^2$ as L_r increases. In fact, the following result holds true when L_r grows unboundedly.

Corollary 1. *If $L_r \rightarrow \infty$ then*

$$H_{nm} \rightarrow \begin{cases} \sqrt{L_s} G_n, & n = m \\ 0 & n \neq m \end{cases} \quad (65)$$

with

$$G_n = G_z \left(\frac{2\pi}{L_s} \left(n - 1 - \frac{N-1}{2} \right), d \right). \quad (66)$$

Proof: If $L_r \rightarrow \infty$ then

$$\frac{1}{2\pi} \Psi_n(\kappa_z) \rightarrow \delta \left(\kappa_z - 2\pi \frac{n - 1 - (N-1)/2}{L_s} \right). \quad (67)$$

By using the above result into (63) yields

$$H_{nm} \rightarrow \sqrt{L_s} G_n \text{sinc}(n - m) \quad (68)$$

where G_n in (66) is obtained from (63) by taking $\kappa_z = \frac{2\pi}{L_s}(n-1-(N-1)/2)$. Since $\text{sinc}(n-m)$ is 1 for $n = m$ and 0 otherwise, the proof is completed. ■

The above corollary shows that asymptotically $H_{nn}/\sqrt{L_s}$ tends to G_n . Since $G_z(\kappa_z, d)$ is band-limited with bandwidth $\Omega = 2\pi/\lambda$, the maximum dimension of the input signal space depends on the wavenumber spectrum and is given by

$$N_{\max} = 2 \left\lfloor \frac{L_s}{\lambda} \right\rfloor + 1 \quad (69)$$

which corresponds to the maximum DoF of the electromagnetic channel in the 1D setup in Assumption 1; e.g., [24]. If the 3-dB bandwidth is considered, then the approximate dimension reduces to $\lfloor \alpha N_{\max} \rfloor$ with $\alpha = 0.6075$. Recalling that H_{nm} represents the coupling coefficient between source mode m and reception mode n , the above corollary shows that the communication modes are decoupled only when L_r grows to infinity, i.e., when an infinitely large receiving segment is used. This is a direct consequence of the fact that $g_z(z, d)$ is not limited in the spatial-domain. However, the following result can be proved.

Corollary 2. *If $|g_z(z, d)|$ is much smaller than $|g_z(0, d)|$ for $|z| \geq z_g$, i.e.,*

$$|g_z(z, d)| \ll |g_z(0, d)| \quad |z| \geq z_g \quad (70)$$

then

$$L_r \geq L_s + z_g \quad (71)$$

guarantees (65).

Proof: See Appendix C. ■

The above corollary shows that the orthogonality condition (65) can be achieved if L_r is larger than a predefined value z_g for which $|g_z(z, d)|$ in (56) is negligible for $|z| \geq z_g$. Notice that (71) can be viewed as the spatial-counterpart of the time-domain condition (40) in OFDM systems. In other words, the extra length $L_r - L_s \geq z_g$ allows to observe the received signal over its entire support in the spatial-domain. As proved in Appendix C, this restores the orthogonality among the communication modes and basically converts the spatial-domain dispersive channel into a set of flat channels in the wavenumber-domain. Numerical results will show that the asymptotic orthogonality condition (65) is sufficiently accurate starting from a receiver size L_r of the same order of the distance d from the source.

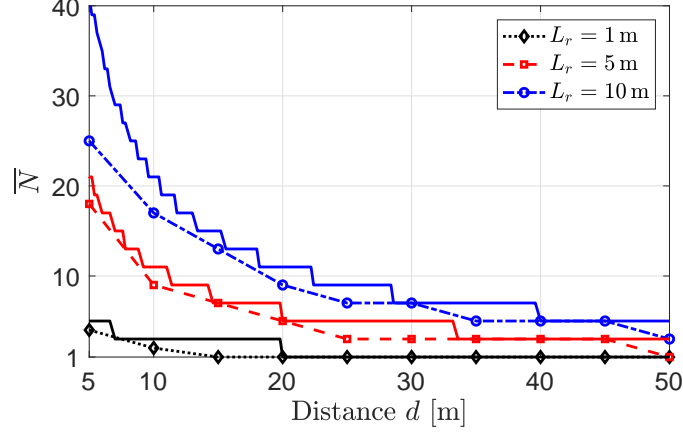


Fig. 7: Number \bar{N} of coupling coefficients H_{nm} that resides in the 3-dB bandwidth of $G_z(\kappa_z, d)$. The solid curves are obtained by using (90) with $L_s = 0.2$ m and $\lambda = 0.01$ m.

Remark 2. Fig. 7 shows that \bar{N} tends to 1 as d increases for any size L_r . Notice that when d grows large and L_r, L_s, λ are kept fixed, we can approximate $g_z(z, d)$ as

$$g_z(z, d) \approx \frac{1}{4\pi} \frac{e^{j\kappa d}}{d} \quad (72)$$

which corresponds to the Green's function in the far-field of source and receiver. This is valid for the propagation range at which the direction and channel gain are approximately the same.

In these circumstances, (55) reduces to

$$H_{nm} = \frac{1}{4\pi} \frac{e^{j\kappa d}}{d} \int_{-\frac{L_r}{2}}^{\frac{L_r}{2}} \psi_n^*(r_x) dr_x \int_{-\frac{L_s}{2}}^{\frac{L_s}{2}} \phi_m(s_x) ds_x \quad (73)$$

from which it follows

$$H_{nm} = \begin{cases} \frac{1}{4\pi} \frac{e^{j\kappa d}}{d} L_r \sqrt{L_s}, & n = m = (N - 1)/2 + 1 \\ 0 & \text{otherwise.} \end{cases} \quad (74)$$

In line with classical MIMO results, a single degree-of-freedom is available in the far-field case.

D. The noise samples

From (27), the noise samples are

$$z_n = \int_{-\frac{L_r}{2}}^{\frac{L_r}{2}} \psi_n^*(r_z) n(d, 0, r_z) dr_z \quad (75)$$

and the matrix \mathbf{R} in (29) has entries

$$[\mathbf{R}]_{nm} = \iint_{-\frac{L_r}{2}}^{\frac{L_r}{2}} \rho(r_z - r'_z) \psi_n^*(r_z) \psi_m(r'_z) dr_z dr'_z \quad (76)$$

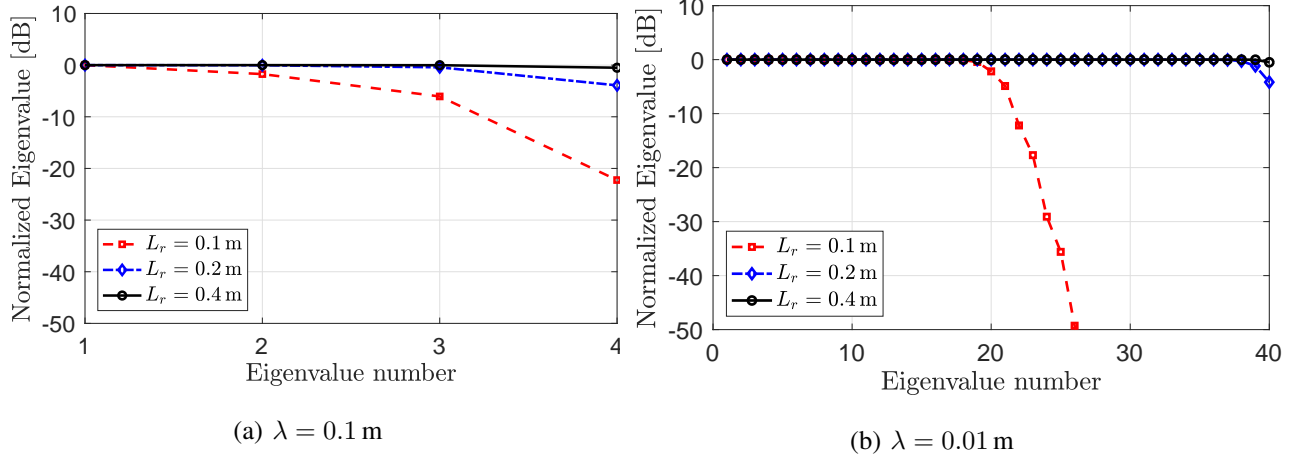


Fig. 8: Normalized eigenvalues in dB of \mathbf{R} when $L_s = 0.2$ m and $L_r = 0.1, 0.2$ and 0.4 m with $\lambda = 0.1$ and 0.01 m.

where $\rho(r_z - r'_z) = \text{sinc}\left(2\frac{r_z - r'_z}{\lambda}\right)$ as it follows from (21) under Assumption 1. The double-integral in (76) can be computed by following the same steps used in Appendix B for the computation of (55). As done for (55), we may rewrite (76) as

$$[\mathbf{R}]_{nm} = \frac{1}{2\pi} \int_{-\infty}^{\infty} S_z(\kappa_z) \Psi_n^*(\kappa_z) \Psi_m(\kappa_z) d\kappa_z \quad (77)$$

where

$$S_z(\kappa_z) = \frac{\pi}{\kappa} \text{rect}\left(\frac{\kappa_z}{2\kappa}\right) = \frac{\lambda}{2} \text{rect}\left(\frac{\kappa_z}{2\kappa}\right) \quad (78)$$

is the wavenumber Fourier transform of $\rho(z)$. This is a rectangular function of bandwidth κ . Hence, the noise samples $\{z_n\}$ are correlated despite the isotropic nature of the electromagnetic noise $\mathbf{n}(\mathbf{r})$. This is a direct consequence of the finite size of L_r that limits the observation interval of $\mathbf{n}(\mathbf{r})$ in the spatial domain. To quantify the spatial correlation properties of noise samples $\{z_n\}$, Fig. 8 plots the normalized eigenvalues in dB of \mathbf{R} when $L_s = 0.2$ m. We consider either $\lambda = 0.1$ m or $\lambda = 0.01$ m corresponding to $N_{\max} = 4$ and $N_{\max} = 40$, respectively. In both cases, we see that the eigenvalues are different only when L_r is small while they become all equal as $L_r \geq 0.4$ m.

The following asymptotic result is obtained.

Corollary 3. *If $L_r \rightarrow \infty$, then*

$$\sigma^2 \frac{[\mathbf{R}]_{nm}}{L_r} \rightarrow \begin{cases} \frac{\sigma^2}{2\kappa}, & n = m \\ 0 & n \neq m \end{cases} \quad (79)$$

for $n \leq 2L_s/\lambda$.

Proof: It follows from (77) by using (78) and the same steps in the proof of Corollary 1. ■

The implication of the above corollary is that, as L_r grows large, the covariance matrix \mathbf{R} becomes diagonal with elements given by $\frac{L_r}{2\kappa}$; that is, the noise samples $\{z_n\}$ become uncorrelated with a variance that increases unboundedly. In practice, this unbounded behaviour of the noise variance is a consequence of the model in Section III-B, which becomes not physically meaningful in the asymptotic regime as it results into noise samples of infinite power. Moreover, it would asymptotically lead to a communication system characterized by a null spectral efficiency since Corollary 1 showed that the coupling coefficients tend to a finite quantity as $L_r \rightarrow \infty$. However, we anticipate that all this is not an issue since the asymptotic orthogonality condition in Corollary 1 is sufficiently accurate for $L_r \geq d$. Hence, in scenarios of practical relevance, the noise variance will be large but always finite, and the noise model from Section III-B can be safely used.

V. SPECTRAL EFFICIENCY

There is a clear analogy between the WDM scheme described above and OFDM. In both cases, Fourier transform operations are applied to convert a matrix channel into a set of parallel independent sub-channels. In OFDM, this is achieved for any finite observation interval T_r that satisfies (40). On the other hand, the orthogonality and independence conditions among communication modes is achieved with WDM only when $L_r \rightarrow \infty$. This implies that, for finite values of L_r , the SVD architecture is needed to decompose the channel into non-interfering and independent single-input single-output channels. Next, we consider two different WDM schemes, i.e., with and without the SVD of $\tilde{\mathbf{H}}$, and make comparisons in terms of spectral efficiency. In doing so, we impose the following constraint

$$\frac{1}{L_s} \int_{-\frac{L_s}{2}}^{\frac{L_s}{2}} |i(s_z)|^2 ds_z \leq P_s \quad (80)$$

and define the system SNR as

$$\text{snr} = \frac{1}{\sigma^2} \frac{1}{L_s} \sum_{n=1}^N |x_n|^2 \stackrel{(a)}{=} \frac{(\kappa Z_0)^2}{\sigma^2} \frac{1}{L_s} \sum_{n=1}^N |\xi_n|^2 \stackrel{(b)}{\leq} \frac{P}{\sigma^2} \quad (81)$$

where (a) follows from (26) and (b) from $\sum_{n=1}^N |\xi_n|^2 / L_s \leq P_s$, as obtained by plugging (45) into (80) and defining $P = (\kappa Z_0)^2 P_s$. Notice that P_s is measured in $[\text{A}^2]$ and P in $[\text{V}^2/\text{m}^2]$.

A. With Singular-Value Decomposition

As any MIMO system, the capacity of WDM is given by (4) and it can be achieved via the transceiver architecture in Fig. 2. This requires the SVD of $\tilde{\mathbf{H}} = \mathbf{L}^{-1}\mathbf{H}$ where \mathbf{H} is the electromagnetic MIMO channel with coupling coefficients as in (55) or (62), and \mathbf{L} is obtained from the Cholesky decomposition of the covariance matrix of $\mathbf{z} = [z_1, \dots, z_N]^T \sim \mathcal{N}_{\mathbb{C}}(\mathbf{0}_N, \sigma^2 \mathbf{R})$ where the elements of \mathbf{R} are given by (76). From Fig. 8, it follows that \mathbf{R} can be well-approximated by a diagonal matrix since the noise samples become uncorrelated for practical values of L_r ; that is, the whitening transformation in Fig. 2 reduces to a simple scaling operation. Notice also that \mathbf{H} can be precomputed in the considered free-space propagation conditions. Particularly, \mathbf{H} is a deterministic matrix, whose computation requires knowledge of the Green's function and the Fourier basis functions $\{\phi_m(\mathbf{s}); m = 1, \dots, N\}$ and $\{\psi_n(\mathbf{r}); n = 1, \dots, N\}$ given by (46) and (52), respectively. They all depend on the system parameters, e.g., wavelength λ , distance d , sizes L_s and L_r . The same is true for the computation of \mathbf{R} , which requires knowledge of the noise power density σ^2 . Notice also that \mathbf{H} and \mathbf{R} are square matrices of size N , i.e., the dimension of the input signal space or, equivalently, the number of communication modes. Since $N \leq N_{\max} = 2L_s/\lambda$, it follows that the maximum number of complex operations required for pre-processing \mathbf{x} and post-processing \mathbf{y} (through $\tilde{\mathbf{V}}$ and $\tilde{\mathbf{U}}$, respectively), is $2N_{\max}^2$. This is an affordable complexity for scenarios of practical interest. Particularly, if $\lambda = 0.01$ m, then $N_{\max} = 40$ and $N_{\max} = 100$ for $L_s = 0.2$ m and $L_s = 0.5$ m. It increases to $N_{\max} = 400$ and $N_{\max} = 1000$ if $\lambda = 0.001$ m.

B. With Linear Processing at the Receiver only

A different scheme is considered here, which does not perform any pre-processing at the source, i.e., $\tilde{\mathbf{V}} = \mathbf{I}_N$, while it still applies linear processing at the receiver with $\tilde{\mathbf{U}} = [\tilde{\mathbf{u}}_1^H, \dots, \tilde{\mathbf{u}}_N^H]^H$. In this case, $\tilde{\mathbf{y}} = \tilde{\mathbf{U}}\mathbf{L}^{-1}\mathbf{y}$, $\mathbf{x} = \tilde{\mathbf{x}}$, and $\tilde{\mathbf{z}} = \tilde{\mathbf{U}}\mathbf{L}^{-1}\mathbf{z}$ has independent and identically distributed Gaussian entries with $\tilde{z}_n \sim \mathcal{N}(0, \sigma_n^2)$ and $\sigma_n^2 = \sigma^2 \|\tilde{\mathbf{u}}_n\|^2$. In scalar form, we obtain

$$\tilde{y}_n = \underbrace{\tilde{\mathbf{u}}_1^H \tilde{\mathbf{h}}_n x_n}_{\text{desired signal}} + \underbrace{\sum_{m=1, m \neq n}^N \tilde{\mathbf{u}}_1^H \tilde{\mathbf{h}}_m x_m}_{\text{interference}} + \tilde{z}_n \quad (82)$$

where $\tilde{\mathbf{H}} = [\tilde{\mathbf{h}}_1^H, \dots, \tilde{\mathbf{h}}_N^H]^H$. Assume that $x_n \sim \mathcal{CN}(0, p_n)$ and that the decoding is performed by treating the interference as Gaussian noise. For any fixed power set $\{p_n; n = 1, \dots, N\}$, the

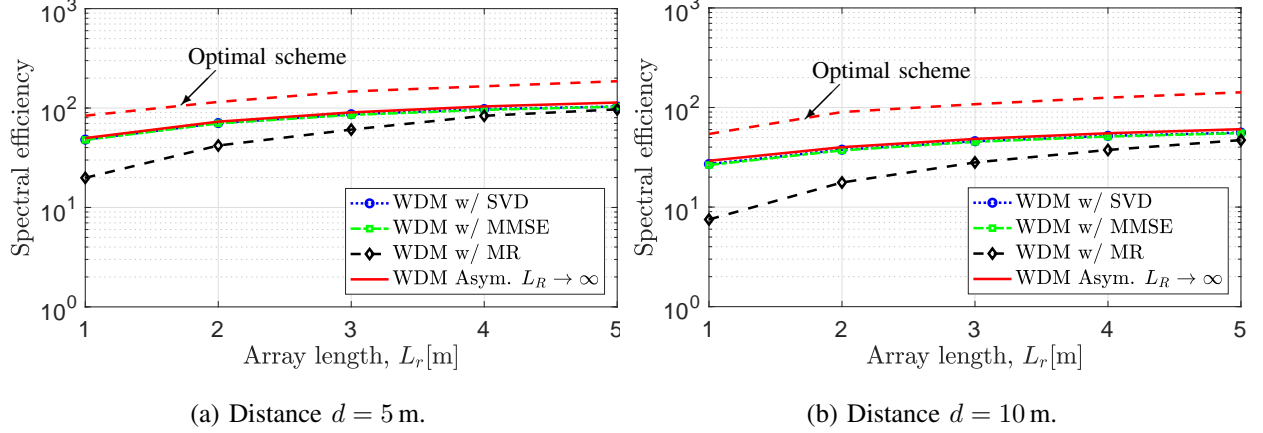


Fig. 9: Spectral efficiency of WDM in bit per channel use. The number of communication modes is (90), as obtained with the paraxial approximation. The asymptotic curve refers to a system in which $L_r \rightarrow \infty$.

spectral efficiency of this communication system is (measured in bit per channel use)

$$SE = \sum_{n=1}^N \log_2(1 + \text{SINR}_n) \quad (83)$$

where

$$\text{SINR}_n = \frac{|\tilde{\mathbf{u}}_n^H \tilde{\mathbf{h}}_n|^2 p_n}{\sum_{m=1, m \neq n}^N |\tilde{\mathbf{u}}_n^H \tilde{\mathbf{h}}_m|^2 p_m + \sigma^2 \tilde{\mathbf{u}}_n^H \tilde{\mathbf{u}}_n} \quad (84)$$

is the signal-to-interference-plus-noise ratio (SINR). This is a generalized Rayleigh quotient with respect to $\tilde{\mathbf{u}}_n$ and thus is maximized by the MMSE combiner, i.e.,

$$\tilde{\mathbf{u}}_n^{\text{MMSE}} = \left(\sum_{m=1}^N p_m \tilde{\mathbf{h}}_m \tilde{\mathbf{h}}_m^H + \sigma^2 \tilde{\mathbf{I}}_N \right)^{-1} \tilde{\mathbf{h}}_n. \quad (85)$$

From Corollary 1, we know that the interference in (84) vanishes as L_r grows large. In this case, MMSE reduces to maximum ratio (MR) combining, i.e., $\tilde{\mathbf{u}}_n^{\text{MR}} = \tilde{\mathbf{h}}_n$, which has lower computational complexity and maximizes the power of the desired signal; that is, it is optimal in a noise-limited regime.

The powers that maximize (84) can be obtained by means of the iterative waterfilling algorithm, whose convergence is not always guaranteed as it depends on the amount of interference (e.g., [25]). To overcome this problem, we exploit Corollary 1 and assume that L_r is sufficiently

large such that the interference in (84) is reasonably smaller than the desired signal. In this case, the optimal powers can be computed as

$$p_n^* = \left(\mu - \frac{\sigma^2}{\|\tilde{\mathbf{h}}_n\|^2} \right)^+ \quad (86)$$

with $\sum_{n=1}^N p_n^* = P$. Unlike (5), the waterfilling solutions (86) are computed with respect to the coupling coefficients $\{\|\tilde{\mathbf{h}}_n\|^2; n = 1, \dots, N\}$. In addition, if the communications modes are transmitted over a wavenumber interval for which the absolute values of the coupling coefficients $\{H_{nn} : n = 1, \dots, N\}$ are nearly constant (as shown in Fig. 6), then (86) reduces to a uniform power allocation.

C. Numerical analysis

Numerical results are used to quantify the spectral efficiency of WDM. We assume $L_s = 0.2$ [m] and $\lambda = 0.01$ [m]. The maximum number of communication modes is $N_{\max} = 2L_s/\lambda = 40$ with spacing in the wavenumber domain of $2\pi/L_s = 31.41$ rad/m. The system SNR given by (81) is $\text{snr} = 70$ dB and the source power is $P_s = 10^{-7}$ [A²]. Accordingly, from Section III-D we have that the radiated power in (30) is $P_{\text{rad}} \leq 3.7 \times 10^{-3}$ [W/m] and the noise power density is $\sigma^2 = 5.6 \times 10^{-4}$ [V²/m²]. Comparisons are made with a communication system in which the basis sets $\{\phi_m(\mathbf{s}); m = 1, \dots, N\}$ and $\{\psi_n(\mathbf{r}); n = 1, \dots, N\}$ are chosen as the eigenfunctions of channel operators. This is reported as a reference. As discussed in Section IV, this requires to select $\phi_n(s_z)$ in (46) as the solution of the following eigenfunction problem:

$$\gamma_n \phi_n(s_z) = \int_{-L_s/2}^{L_s/2} K_s(s_z, s'_z) \phi_n(s'_z) ds'_z \quad (87)$$

with

$$K_s(s_z, s'_z) = \int_{-L_r/2}^{L_r/2} g_z^*(r_z - s_z, d) g_z(r_z - s'_z, d) dr_z. \quad (88)$$

The output basis function in (52) are then obtained as

$$\psi_n(r_z) = \int_{-L_r/2}^{L_r/2} g_z(r_z - s_z, d) \phi_n(s_z) ds_z. \quad (89)$$

Fig. 9 plots the spectral efficiency as a function of L_r when $d = 5$ and 10 m. According to (1), we assume that the number of communication modes is

$$N = 2 \left\lfloor \frac{1}{2} \frac{L_s L_r}{\lambda d} \right\rfloor + 1. \quad (90)$$

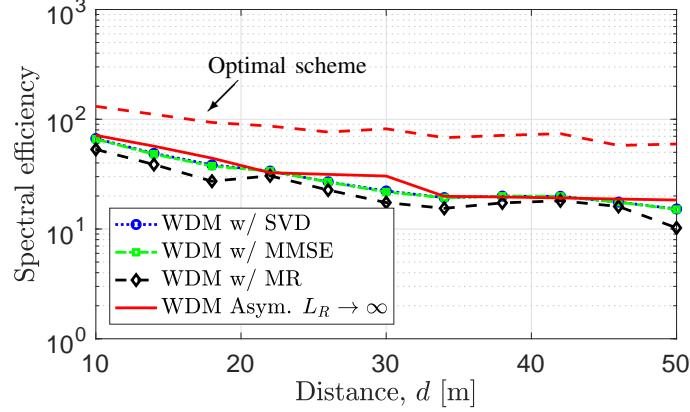


Fig. 10: Spectral efficiency of WDM in bit per channel use as a function of distance when $L_r = 5$ m.

We see that the spectral efficiency of WDM with SVD and MMSE processing is exactly the same and matches well the asymptotic performance (i.e., free-interference case) for any value of L_r . On the contrary, WDM with MR processing approaches the asymptotic performance only when L_r is large. As a rule of thumb, this is approximately achieved by $L_r \geq d$. Compared to the optimal scheme, a substantial loss is observed. However, we recall that the superior performance of the optimal scheme is achieved at the cost of a prohibitively high implementation complexity. Fig. 10 plots the spectral efficiency as a function of the distance. We see that WDM with SVD and MMSE processing performs very close irrespective of the distance. The spectral efficiency reduces as d increases since the received power as well as the number of communication modes decreases.

VI. CONCLUSIONS AND FUTURE RESEARCH DIRECTIONS

Building on prior analyses (e.g., [8]–[10]), we provided a MIMO representation of the electromagnetic wave propagation problem between two spatially-continuous volumes, which can be directly used by communication theorists as a baseline for developing and studying optimal or suboptimal (but implementable) holographic MIMO communication schemes. Particularly, we used it to develop a communication scheme for the system setup in Fig. 1; that is, linear sources and receivers in LoS propagation conditions. Inspired by OFDM, we made use of Fourier basis functions and proposed a WDM communication scheme that operates in the wavenumber domain and makes use of Fourier transform operations directly at the electromagnetic level. Conventional tools of linear systems theory were used to understand the interplay among the different system

parameters in terms of number of communication modes and level of interference. Unlike OFDM, the orthogonality among the communication modes (in the wavenumber domain) is achieved with WDM only when the size of the receiver grows infinitely large, due to the unbounded support of the channel response in the spatial domain. Different communication architectures were thus used and designed to deal with the interference. Numerical results showed that, for the investigated scenarios, the optimal SVD architecture with water-filling and the linear MMSE receiver with suboptimal power allocation achieve the same spectral efficiency of the interference-free case (infinitely large receiver), while MR combining processing performs sufficiently well starting from a receiver size of the same order of the distance from the source.

Future research directions for the proposed WDM scheme are clearly represented by considering scenarios where some of the underlying assumptions of Fig. 1 are not valid. A first extension is to study the effects of multipath propagation and LoS blockage. Since in practice the source and receiver are not parallel, the impact of arbitrary positions and orientations should be investigated. This would open the door for multi-user communications in which multiple sources (arbitrarily located in the area) transmit to a fixed receiver. A natural extension is also the design of the WDM scheme when two-dimensional (rather one-dimensional) surfaces are used for transmission and reception [16]; this provides additional flexibility in terms of generating the current densities and processing the impinging electric fields.

APPENDIX A

From [23, Ch. 14], the radiated power P_{rad} is given by $P_{\text{rad}} = \lim_{r \rightarrow \infty} \int_{\Omega} P_r r^2 d\Omega$ where

$$P_r = \frac{1}{2Z_0} \mathbf{e}^H(\mathbf{r}) \mathbf{e}(\mathbf{r}) \quad (91)$$

is the radial component of the Poynting vector [23, Ch. 14], $\mathbf{e}(\mathbf{r})$ is the *radiation* electric field with $r = \|\mathbf{r}\|$, and Ω is the solid angle of 4π steradians. When $r \rightarrow \infty$, the electric field reduces to

$$\mathbf{e}(\mathbf{r}) = j\kappa Z_0 \frac{e^{j\kappa r}}{4\pi r} (\mathbf{I} - \widehat{\mathbf{r}}\widehat{\mathbf{r}}^H) \int_{V_s} \mathbf{j}(\mathbf{s}) e^{-j\kappa^T(\theta_s, \varphi_s)\mathbf{s}} d\mathbf{s} \quad (92)$$

since the Green's function (13) can be approximated as

$$\mathbf{g}(\mathbf{r}, \mathbf{s}) \approx \frac{1}{4\pi} \frac{e^{j\kappa r}}{r} (\mathbf{I} - \widehat{\mathbf{r}}\widehat{\mathbf{r}}^H) e^{-j\kappa^T(\theta_s, \varphi_s)\mathbf{s}}. \quad (93)$$

Plugging (92) into (91) yields

$$P_r = \frac{Z_0}{8\lambda^2} \frac{1}{r^2} \left\| (\mathbf{I} - \widehat{\mathbf{r}}\widehat{\mathbf{r}}^H) \int_{V_s} \mathbf{j}(\mathbf{s}) e^{-j\kappa^T(\theta_s, \varphi_s)\mathbf{s}} d\mathbf{s} \right\|^2 \leq \frac{Z_0}{8\lambda^2} \frac{1}{r^2} \left\| \int_{V_s} \mathbf{j}(\mathbf{s}) e^{-j\kappa^T(\theta_s, \varphi_s)\mathbf{s}} d\mathbf{s} \right\|^2. \quad (94)$$

From (94), we thus have that P_{rad} can be upper bounded as

$$P_{\text{rad}} \leq \frac{Z_0}{8\lambda^2} \int_{\Omega} \left\| \int_{V_s} \mathbf{j}(\mathbf{s}) e^{-j\boldsymbol{\kappa}^T(\theta_s, \varphi_s)\mathbf{s}} d\mathbf{s} \right\|^2 d\Omega = 4\pi \frac{Z_0}{8\lambda^2} \iint_{V_s} \mathbf{j}^H(\mathbf{s}_1) \mathbf{j}(\mathbf{s}_2) \rho(\mathbf{s}_1 - \mathbf{s}_2) d\mathbf{s}_1 d\mathbf{s}_2$$

where $\rho(\cdot)$ is given in (21). By applying the Cauchy-Schwarz inequality, we obtain (30).

APPENDIX B

Rewrite the integral in (55) as $H_{nm} = A_1 + A_2 + A_3$ with

$$A_1 = \int_{-L_r/2-L_s/2}^{-L_r/2+L_s/2} f_m(x) \left(\int_{-L_r/2}^{L_s/2+x} e^{j2\pi(m-n)r/L_s} dr \right) dx \quad (95)$$

$$A_2 = \int_{-L_r/2+L_s/2}^{L_r/2-L_s/2} f_m(x) \left(\int_{-L_s/2+x}^{L_s/2+x} e^{j2\pi(m-n)r/L_s} dr \right) dx \quad (96)$$

$$A_3 = \int_{L_r/2-L_s/2}^{L_r/2+L_s/2} f_m(x) \left(\int_{-L_s/2+x}^{L_r/2} e^{j2\pi(m-n)r/L_s} dr \right) dx \quad (97)$$

with $f_m(x) = \frac{1}{\sqrt{L_s}} g(x) e^{-j2\pi mx/L_s}$. If $n = m$, then

$$A_1 = \int_{-L_r/2-L_s/2}^{-L_r/2+L_s/2} f_m(x) \left(\frac{L_s + L_r}{2} + x \right) dx \quad (98)$$

$$A_2 = \int_{-L_r/2+L_s/2}^{L_r/2-L_s/2} f_m(x) L_s dx \quad (99)$$

$$A_3 = \int_{L_r/2-L_s/2}^{L_r/2+L_s/2} f_m(x) \left(\frac{L_s + L_r}{2} - x \right) dx. \quad (100)$$

If $n \neq m$, then $A_2 = 0$ and

$$A_1 = b_{nm} \int_{-L_r/2-L_s/2}^{-L_r/2+L_s/2} f_m(x) c_{nm}(x) dx \quad (101)$$

$$A_3 = -b_{nm} \int_{L_r/2-L_s/2}^{L_r/2+L_s/2} f_m(x) c_{nm}(x) dx \quad (102)$$

with $b_{nm} = \frac{L_s}{j2\pi(m-n)}$ and $c_{nm}(x) = (-1)^{m-n} e^{j2\pi(m-n)\frac{x}{L_s}} - e^{-j\pi(m-n)\frac{L_r}{L_s}}$. Notice that the above steps can also be used for the computation of the elements of \mathbf{R} in (76), after taking into account that $\psi_n(s_x)$ must be replaced with $\phi_m(s_x)$.

APPENDIX C

Define $\frac{\kappa'_z}{2\pi} = \frac{\kappa_z}{2\pi} - \frac{m-1-(N-1)/2}{L_s}$ and rewrite the integral in (62) as follows

$$\int_{-\infty}^{\infty} G_z \left(\kappa'_z + 2\pi \frac{m-1-(N-1)/2}{L_s}, d \right) Q_{n-m}(\kappa'_z) d\kappa'_z \quad (103)$$

with

$$Q_i(\kappa'_z) = \text{sinc} \left(\frac{\kappa'_z}{2\pi} L_s \right) \text{sinc} \left(\left(\frac{\kappa'_z}{2\pi} + \frac{i}{L_s} \right) L_r \right). \quad (104)$$

By using Parseval, (103) becomes

$$\int_{-\infty}^{\infty} g_z(z', d) e^{j2\pi \frac{m-1-(N-1)/2}{L_s} z'} q_{n-m}(z') dz' \quad (105)$$

with

$$q_i(z') = \frac{(2\pi)^2}{L_s L_r} \text{rect} \left(\frac{z'}{L_s} \right) \otimes \text{rect} \left(\frac{z'}{L_r} \right) e^{-j \frac{2\pi}{L_s} i z'}. \quad (106)$$

Assume now that the conditions in (70) and (71) are satisfied. In these circumstances, the integral in (105) reduces to

$$\int_{-z_g}^{z_g} g_z(z', d) e^{j2\pi \frac{m-1-(N-1)/2}{L_s} z'} q_{n-m}(z') dz'. \quad (107)$$

For $|z'| \leq z_g$, it is easy to show that $q_i(x') = \frac{(2\pi)^2}{L_r}$ for $i = 0$ and $q_i(x') = 0$ for $i \neq 0$. Plugging this result into (107) produces

$$\begin{cases} \frac{(2\pi)^2}{L_r} \int_{-z_g}^{z_g} g_z(z', d) e^{j2\pi \frac{n-1-(N-1)/2}{L_s} x'} dz' & n = m \\ 0 & n \neq m. \end{cases} \quad (108)$$

By noticing that, under the condition in (71),

$$\int_{-z_g}^{z_g} g_z(z', d) e^{j2\pi \frac{n-1-(N-1)/2}{L_s} z'} dz' = G_z \left(\frac{2\pi}{L_s} (n - N/2 - 1), d \right) \quad (109)$$

the orthogonality condition in (65) easily follows.

REFERENCES

- [1] T. S. Rappaport, Y. Xing, O. Kanhere, S. Ju, A. Madanayake, S. Mandal, A. Alkhateeb, and G. C. Trichopoulos, "Wireless communications and applications above 100 ghz: Opportunities and challenges for 6G and beyond," *IEEE Access*, vol. 7, pp. 78 729–78 757, 2019.
- [2] D. Tse and P. Viswanath, *Fundamentals of Wireless Communication*. Cambridge University Press, 2005.
- [3] P. Driessen and G. Foschini, "On the capacity formula for multiple input-multiple output wireless channels: a geometric interpretation," *IEEE Trans. Commun.*, vol. 47, no. 2, pp. 173–176, 1999.
- [4] J.-S. Jiang and M. Ingram, "Spherical-wave model for short-range MIMO," *IEEE Trans. Commun.*, vol. 53, no. 9, 2005.

- [5] F. Bohagen, P. Orten, and G. E. Oien, "On spherical vs. plane wave modeling of line-of-sight MIMO channels," *IEEE Trans. Commun.*, vol. 57, no. 3, pp. 841–849, 2009.
- [6] E. Torkildson, U. Madhow, and M. Rodwell, "Indoor millimeter wave MIMO: Feasibility and performance," *IEEE Trans. Wireless Commun.*, vol. 10, no. 12, pp. 4150–4160, 2011.
- [7] H. Do, N. Lee, and A. Lozano, "Reconfigurable ULAs for line-of-sight MIMO transmission," *IEEE Trans. Wireless Commun.*, vol. 20, no. 5, pp. 2933–2947, 2021.
- [8] D. A. B. Miller, "Communicating with waves between volumes: evaluating orthogonal spatial channels and limits on coupling strengths," *Appl. Opt.*, vol. 39, no. 11, pp. 1681–1699, Apr 2000.
- [9] F. K. Gruber and E. A. Marengo, "New aspects of electromagnetic information theory for wireless and antenna systems," *IEEE Trans. Antennas Propag.*, vol. 56, no. 11, pp. 3470–3484, 2008.
- [10] M. A. Jensen and J. W. Wallace, "Capacity of the continuous-space electromagnetic channel," *IEEE Transactions on Antennas and Propagation*, vol. 56, no. 2, pp. 524–531, 2008.
- [11] M. Franceschetti, *Wave Theory of Information*. Cambridge University Press, 2017.
- [12] A. Pizzo, L. Sanguinetti, and T. L. Marzetta, "Holographic MIMO communications," *CoRR*, vol. abs/2105.01535, 2021. [Online]. Available: <https://arxiv.org/abs/2105.01535>
- [13] D. Dardari and N. Decarli, "Holographic Communication using Intelligent Surfaces," *CoRR*, vol. abs/2012.01315, 2020. Online: <https://arxiv.org/abs/2012.01315>.
- [14] C. Huang, S. Hu, G. C. Alexandropoulos, A. Zappone, C. Yuen, R. Zhang, M. D. Renzo, and M. Debbah, "Holographic MIMO surfaces for 6g wireless networks: Opportunities, challenges, and trends," *IEEE Wireless Communications*, vol. 27, no. 5, pp. 118–125, 2020.
- [15] D. Slepian, "Prolate spheroidal wave functions, Fourier analysis and uncertainty: Extensions to many dimensions; generalized prolate spheroidal functions," *The Bell System Technical Journal*, vol. 43, no. 6, pp. 3009–3057, 1964.
- [16] D. Dardari, "Communicating with large intelligent surfaces: Fundamental limits and models," *IEEE J. Sel. Areas Commun.*, vol. 38, no. 11, pp. 2526–2537, 2020.
- [17] S. Tretyakov, "Metasurfaces for general transformations of electromagnetic fields," *Philosophical Trans. Royal Soc. A: Mathematical, Physical and Engineering Sciences*, vol. 373, no. 2049, 2015.
- [18] Y. B. Li, B. G. Cai, Q. Cheng, and T. J. Cui, "Surface Fourier-transform lens using a metasurface," *Journal of Physics D: Applied Physics*, vol. 48, no. 3, p. 035107, jan 2015. [Online]. Available: <https://doi.org/10.1088/0022-3727/48/3/035107>
- [19] E. Telatar, "Capacity of multi-antenna gaussian channels," *European Trans. Telecommun.*, vol. 10, no. 6, 1999.
- [20] F. Bohagen, P. Orten, and G. Oien, "Construction and capacity analysis of high-rank line-of-sight MIMO channels," in *IEEE Wireless Commun. Netw. Conf., 2005*, vol. 1, 2005, pp. 432–437 Vol. 1.
- [21] W. C. Chew, *Waves and Fields in Inhomogenous Media*. Wiley-IEEE Press, 1995.
- [22] A. S. Y. Poon, R. W. Brodersen, and D. N. C. Tse, "Degrees of freedom in multiple-antenna channels: a signal space approach," *IEEE Trans. Inf. Theory*, vol. 51, no. 2, Feb 2005.
- [23] S. J. Orfanidis, *Electromagnetic Waves and Antennas*. [Online]. Available: <http://www.ece.rutgers.edu/orfanidi/ewa/>, 2008.
- [24] A. Pizzo, T. L. Marzetta, and L. Sanguinetti, "Degrees of Freedom of Holographic MIMO Channels," in *2020 IEEE 21st Int. Workshop Signal Process. Adv. Wireless Commun. (SPAWC)*, 2020, pp. 1–5.
- [25] W. Yu, W. Rhee, S. Boyd, and J. Cioffi, "Iterative water-filling for gaussian vector multiple-access channels," *IEEE Trans. Inf. Theory*, vol. 50, no. 1, pp. 145–152, 2004.